Supplement of Atmos. Chem. Phys., 26, 2881–2892, 2026
https://doi.org/10.5194/acp-26-2881-2026-supplement

Atmospheric Chemistry and Physics

Supplement of

Effects of mass ratio heterogeneity and coating-related optical characteristics on the light absorption enhancement of black carbon-containing particles

Jing Wei et al.

Correspondence to: Bin-Ye Xu (xubingye@zjemc.org.cn) and Zhi-Bin Wang (wangzhibin@zju.edu.cn)

S1. Correction of CPMA-SP2 data

(1) Correction of delay time. Aerosols are passed through the CPMA for mass selection before being measured by the SP2. Due to differences in tubing length and the response times of the instruments or computers, there exists a time lag between the CPMA and SP2 measurements, which affects the accuracy of their mass correspondence. In addition, the CPMA requires different rotational speeds to select particles of different masses, which leads to a certain response delay during mass switching. Since the time required for rotational speed switching varies between different mass settings, it is difficult to accurately correct for this delay. Therefore, in the data processing, we discard the data from one minute before and one minute after each mass switching event, and only retain the stable 3-minute data in the middle of each mass segment for analysis.

(2) Transfer function calculation. To accurately interpret the CPMA-SP2 measurements, we calculated the mass-dependent CPMA transfer function for each CPMA mass setpoints used in this study. The CPMA was operated in rotational-speed selection mode, with an inner radius r_1=100mm, an outer radius r_2 =103 mm, and an electrode length L =200 mm. The flowrate was maintained at Q=0.42 mL/min. The rotational speed ratio of the CPMA electrodes was ω_2/ω_1=0.945. For each mass setpoint, the particle transmission probability as a function of particle mass M_p were calculated using the CPMA geometric parameters, flow conditions (Sipkens et al., 2020a; Sipkens et al., 2020b). The transmission function was computed using a standard CPMA analytical formula based on the set mass resolution R_m=8:

$$T\left(M_p\right)=\frac{1}{1+\left(\frac{M_p}{M_c}-1\right)^2},\lambda=\frac{\pi}{4ln2}R_m^2 \tag{S1}$$

where M_c is the center mass of the CPMA setpoint. This approach produces unimodal, narrow transmission curves centered at each setpoint mass, with limited overlap between adjacent setpoints. The continuous transmission functions were then discretized by integrating over predefined particle mass bins [M_{p_lower}, M_{p_upper}], generating a kernel for each mass point:

$$K_i=\int_{M_{p\_lower},i}^{M_{p\_upper},i}T\left(M_p\right)dM_p \tag{S2}$$

Fig. S10 shows the calculated CPMA transfer functions, which were subsequently used to construct the kernel matrix for data analysis.

(3) Correction of collection efficiency of SP2.

The correction of sampling efficiency includes detector counting efficiency and tube losses. Before sampling, we measured the detection efficiency of the SP2 detector. The results showed that the counting concentrations of BC particles measured by the SP2 and CPC were generally consistent across different particle sizes. Therefore, this study assumes the counting efficiency of the SP2 detector to be 100%.

Due to Brownian motion, particles with smaller diameters tend to diffuse from regions of high concentration to regions of low concentration and deposit on the inner walls of the tube. In a tube where gas flows under laminar conditions, the particle transmission efficiency η is related to the parameter $\zeta = \frac{\pi DL}{Q}$, where *D* represents the particle diffusion coefficient, *L* is the tube length, and *Q* is the volumetric flow rate of the gas. A mathematical expression was raised to characterize the transmission efficiency of particle deposition under laminar flow conditions (Gormley and Kennedy, 1984).

$$\eta = 1 - 2.56\zeta^{\frac{2}{3}} + 1.2\zeta + 0.177\zeta^{\frac{4}{3}} \quad \zeta < 0.009 \tag{S3}$$

$$\eta = 0.819\exp(-3.657\zeta) + 0.097\exp(-22.3\zeta) + 0.032\exp(-57\zeta) \quad \zeta > 0.009 \tag{S4}$$

According to Equations 2 and 3, the particle transmission efficiency of each M_p bins was showed in Fig. S13a.

(4) Correction of multiple charge. The CPMA selects aerosol particles based on the balance between the centrifugal force and the electric field force,

$$\frac{M_p}{N_q} = \frac{eV}{r^2\omega^2\ln(r_0/r_1)} \tag{S5}$$

where M_p is the particle mass, N_q is the charge on each particle, *e* is the is the elementary charge (1.6×10^{-19}C), r_0 and r_1 are the radii of the inner and outer cylinders, and *r* is the center radius of the two cylinders, *ω* is the angular velocity at this radius.

When CPMA selected large mass aerosols with multiple charges, their mass-to-charge ratio may be similar to that of small mass aerosols with a single charge. To eliminate these large and multiply charged particles, we apply a correction based on their scattering signals. First, we summary the probability distribution of the scattering signals for each mass bin, and further fit the distribution to identify multiply charged particles with larger scattering signals. Only the singly charged particles was retained (Fig. S12). The three-dimensional M_c-M_p distribution before and after correction is also shown in Fig. S11. The scattering signals are fitted using the LEO method.

The charging ability of aerosols decreases with the reduction in particle size. This study is based on the method of limiting spheres developed by Fuchs et al. (1962), and uses convective diffusion and kinetic models to calculate the particle migration rates. Subsequently, the proportion of aerosols with a single charge in each size bin is assessed, with the particle density based on measurements by Zhao et al. (2019) in the field environment. The calculation results are shown in Fig. S13. Based on this, the total number of particles for each mass at different sizes is further obtained.

S2. Uncertainty assessment

(1) The uncertainty of the measured MAC (MAC$_{\text{BC\_coated\_measured}}$):

The MAC$_{\text{BC\_coated\_measured}}$ of BC was calculated as:

$$MAC_{\text{BC\_coated\_measured}} = \frac{\sigma_{abs}}{M_{BC\_core}} \quad \text{(S6)}$$

where σ_{abs} is the absorption coefficient and $M_{\text{BC\_core}}$ is the BC mass. The relative uncertainty of MAC$_{\text{BC\_coated\_measured}}$ was estimated using standard error propagation for independent variables:

$$\frac{\mu_{MAC\_\text{BC\_coated}}}{MAC_{\text{BC\_coated\_measured}}} = \sqrt{\left(\frac{\mu_\sigma}{\sigma_{abs}}\right)^2 + \left(\frac{\mu_M}{M_{BC\_core}}\right)^2} \quad \text{(S7)}$$

where $\frac{\mu_\sigma}{\sigma_{abs}}$ is the relative uncertainty of the absorption coefficient (15%-20%) and $\frac{\mu_M}{M_{BC\_core}}$ is the relative uncertainty of BC mass measured by SP2 (10%). Then the resulting relative uncertainty of MAC$_{\text{BC\_coated\_measured}}$ ($\frac{\mu_{MAC\_\text{BC\_coated}}}{MAC_{\text{BC\_coated\_measured}}}$) was estimated as 18%-22%.

(2) The measurement uncertainty of the MAC for uncoated BC (MAC$_{\text{BC\_core\_meausred}}$)

The MAC of BC core (MAC$_{\text{BC\_core\_meausred}}$) was obtained by extrapolating the measured MAC$_{\text{BC\_coated\_measured}}$ to the limit of bulk-averaged M_{R}=0 using linear regression. The standard error of the regression intercept was 0.53, which corresponds to a relative uncertainty of 5.8% based on the reference MAC value of 9.08 m^2 g^{-1}. Then the total relative uncertainty of MAC$_{\text{BC\_core\_meausred}}$ was calculated as:

$$\frac{\mu_{MAC\_core}}{MAC_{BC\_core\_measured}} = \sqrt{\left(\frac{\mu_\sigma}{\sigma_{abs}}\right)^2 + \left(\frac{\mu_M}{M_{BC\_core}}\right)^2 + \left(\frac{\mu_{fit}}{MAC_{BC\_core\_measured}}\right)^2} \quad \text{(S8)}$$

So, the uncertainty associated with the MAC$_{\text{BC\_core\_meausred}}$ ($\frac{\mu_{MAC\_core}}{MAC_{BC\_core\_measured}}$) was estimated to range from 19-23%.

(3) The uncertainty of the $E_{\text{abs\_measured}}$

The $E_{\text{abs\_measured}}$ was calculated as the ratio of the coated BC MAC to the uncoated BC MAC:

$$E_{abs\_measured} = \frac{MAC_{\text{BC\_coated\_measured}}}{MAC_{BC\_core\_measured}} \quad \text{(S9)}$$

the relative uncertainty of $E_{\text{abs\_measured}}$ was obtained using standard error propagation:

$$\frac{\mu_{Eabs}}{E_{abs\_measured}} = \sqrt{\left(\frac{\mu_{MAC\_\text{BC\_coated}}}{MAC_{\text{BC\_coated\_measured}}}\right)^2 + \left(\frac{\mu_{MAC\_core}}{MAC_{BC\_core\_measured}}\right)^2} \quad \text{(S10)}$$

Based on MAC uncertainties of 18-22% for coated BC and 19-23% for core BC, the resulting relative uncertainty of $E_{\text{abs\_measured}}$ ($\frac{\mu_{Eabs}}{E_{abs\_measured}}$) was estimated to be 26-32%.

(4) The M_{R} uncertainty of single BC-containing particle

The M_R of single BC-containing particle was calculated by $M_\mathrm{R}=(M_\mathrm{p}-M_\mathrm{BC\_core})/M_\mathrm{BC\_core}$, so the corresponding uncertainty can be expressed as:

$$\frac{\mu_{MR}}{M_R} = \sqrt{\left(\frac{\mu_{Mp}}{M_p}\right)^2 + \left(\frac{\mu_{MBC\_core}}{M_{BC\_core}}\right)^2} \qquad \text{(S11)}$$

here, $\frac{\mu_{Mp}}{M_p}$ represents the CPMA mass accuracy uncertainty of 5%, and $\frac{\mu_{MBC\_core}}{M_{BC\_core}}$ is 10%. Therefore, the M_R of single BC-containing particle ($\frac{\mu_{MR}}{M_R}$) was approximately 11%.

(5) The uncertainty of bulk-averaged M_R of BC-containing particles

The bulk-averaged M_R in bulk particles by summing of total coating and core mass of BC-containing particles every M_p bins,

$$bulk - averaged\ M_R = \frac{\sum_i M_{R,i} \times M_{BC\_core,i}}{\sum_i M_{BC\_core,i}} \qquad \text{(S12)}$$

where i was the i^{th} single BC-containing particle. Each M_R of each M_p bins is weighted by its BC mass, with the BC mass fraction of sample i defined as:

$$\omega_i = \frac{M_{BC\_core,i}}{\sum_i M_{BC_{core},i}} \qquad \text{(S13)}$$

The measured BC mass fraction for the selected 8 M_p bins were 0.0711,0.0936, 0.1456, 0.1793, 0.15440.1364, 0.1482, and 0.0713, reflecting the relative contribution of each sample to the bulk-averaged M_R.

The uncertainty of bulk-averaged M_R was estimated using first-order Gaussian error propagation, considering the constant relative uncertainties of $M_\mathrm{R,i}$ (11%) and $M_\mathrm{BC\_core,i}$ (10%). The propagated uncertainty is:

$$\mu_{bulk-averaged\ MR} = \sqrt{\sum_i \left(\omega_i M_{R,i}\right)^2 (11\%^2 + 10\%^2) + bulk - averaged\ M_R^2 \sum_i \omega_i^2 \times 10\%^2} \qquad \text{(S14)}$$

The first term under the square root represents the contribution of each M_p bins' M_R and BC uncertainty weighted by its BC mass, while the second term accounts for the uncertainty associated with the normalization of BC masses. Using the measured BC masses and the assumed relative uncertainties, the relative uncertainty of the bulk-averaged M_R was calculated to be approximately 7%.

Table S1. The abbreviation of this study

Abbreviation	Full Name
BC	Black carbon
E_{abs}	light absorption enhancement
M_R	Coating-to-core mass ratio of single BC-containing particle
DRF	direct radiative forcing
bulk-averaged M_R	Averaged M_R of bulk BC-containing particle
C_{sca}	the scattering cross-section
$C_{sca\_measured}$	the measured scattering cross-section
$C_{sca\_modeled}$	the modeled scattering cross-section by core-shell Mie model
M_p	the mass of a BC-containing particle
M_{BC_core}	the mass of BC core
MAC	the mass absorption cross section
$E_{abs\_measured}$	the measured light absorption enhancement
$MAC_{BC\_core\_measured}$	the MAC of uncoated BC particles extrapolated from measured MAC values of BC-containing particles
D_c	the BC core size
D_p/D_c	BC coating thickness
RI	the refractive index
$MAC_{BC\_coated\_modeled}$	modeled MAC of coated BC
WS	wind speed
RH	relative humidity
$E_{abs\_uniform}$	the E_{abs} calculated using the traditional core-shell Mie model
ΔE_{abs}	$E_{abs\_uniform}$-$E_{abs\_measured}$
$E_{abs\_resolved}$	the E_{abs} calculated from each BC-containing particle using the core-shell Mie model
E_{abs_param}	the E_{abs} obtained based on the empirical scheme developed in this study
CPMA	Centrifugal Particle Mass Analyzer
SP2	single-particle soot photometer
PSL	polystyrene latex spheres
ToF-ACSM X	time-of-flight aerosol chemical speciation monitor
CAPS-ALB	Multi-Wavelength Cavity Attenuated Phase Shift Single-Scattering Albedo Monitor
DMA	Differential Mobility Analyzer
LEO	the leading-edge-only technique

Table S2. Light absorption enhancement of BC at different studies

Number	Site	Bulk averaged-M_R	E_{abs}	Wavelength (nm)	References
1	Beijing	2.60±2.12	1.46±0.44	532	(Peng et al., 2016)
	Houston	1.01±0.46	1.06±0.04	532	
2	Shanghai (high)	4.26±2.92	1.63±0.35	532	(Zhai et al., 2022)
	Shanghai (low)	5.81±2.39	1.29±0.04	532	
3	Shenzhen	4.89±1.05	1.15±0.04	870	(Huang et al., 2024)
4	Fontana	7.46±3.46	1.14±0.08	532	(Cappa et al., 2019)
5	California	9.95±7.01	1.03±0.02	532	(Cappa et al., 2012)

Table S3. The M_R determination range of "transition-state" BC-containing particles at different periods

M_p (fg)	List	Case1	Case2	Case3
2.02	Transition Start	1.5	1.1	1.3
	Transition End	—	—	3.1
2.97	Transition Start	1.9	1.3	1.3
	Transition End	—	—	4.5
4.35	Transition Start	1.7	1.5	1.3
	Transition End	6.2	3.7	4.1
6.39	Transition Start	1.9	1.5	1.4
	Transition End	5.9	4.2	3.9
9.38	Transition Start	1.9	1.6	1.7
	Transition End	6.4	3.1	4.7
13.77	Transition Start	1.8	1.6	1.7
	Transition End	6.7	3.9	4.6
20.22	Transition Start	1.7	—	—
	Transition End	6.5	4.0	4.4
Average	Transition Start	1.78	1.43	1.45
	Transition End	6.34	3.78	4.19

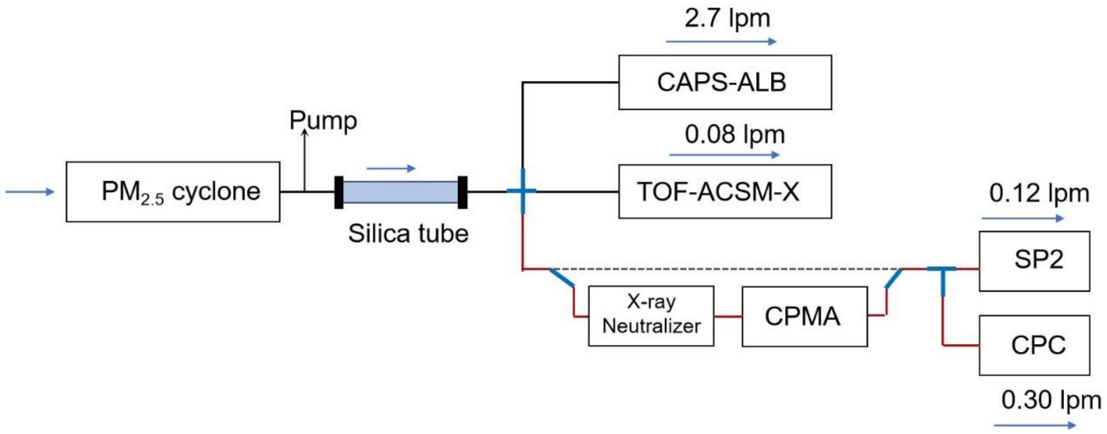

Figure S1. Schematic of the sampling system. The dotted line represents the SP2 sample flow, and the red line represents the CPMA-SP2 tandem system sample flow.

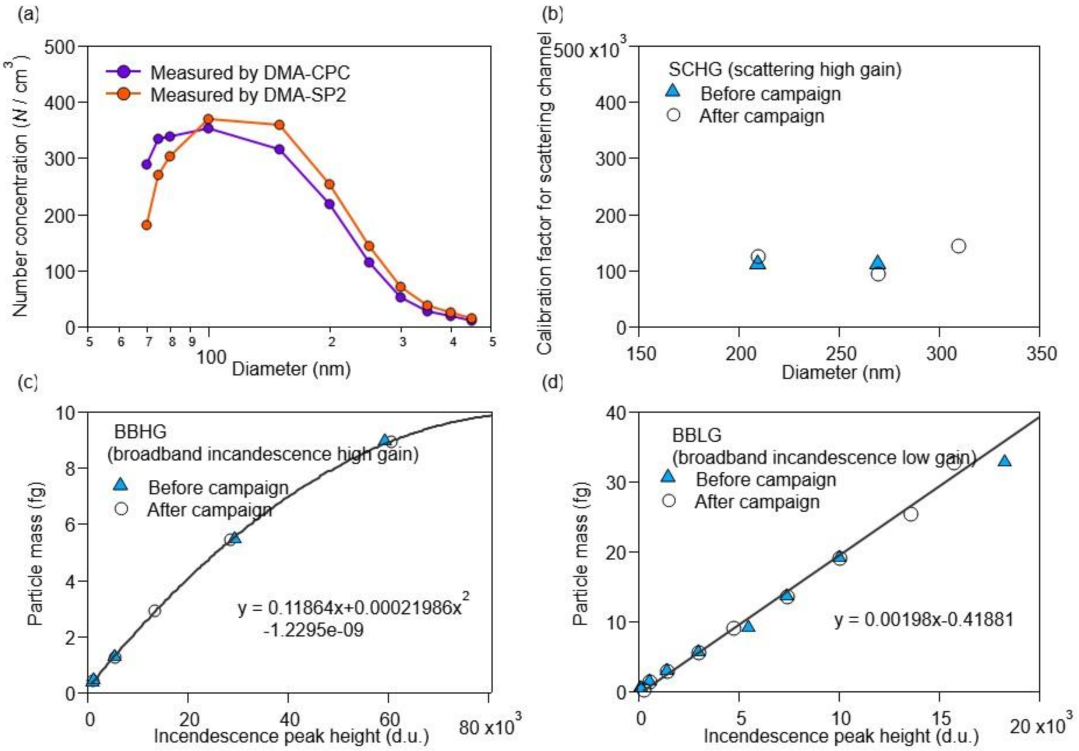

Figure S2. The number concentration measured by SP2 and CPC after DMA classification of size-resolved Aquadag aerosols (a). (b) showed the calibration factor for scattering high gain (SCHG) before and after campaign. (c) and (d) display the correlation between incandescence peak height and BC particle mass at broadband incandescence high gain (BBHG) and broadband incandescence low gain (BBLG), respectively.

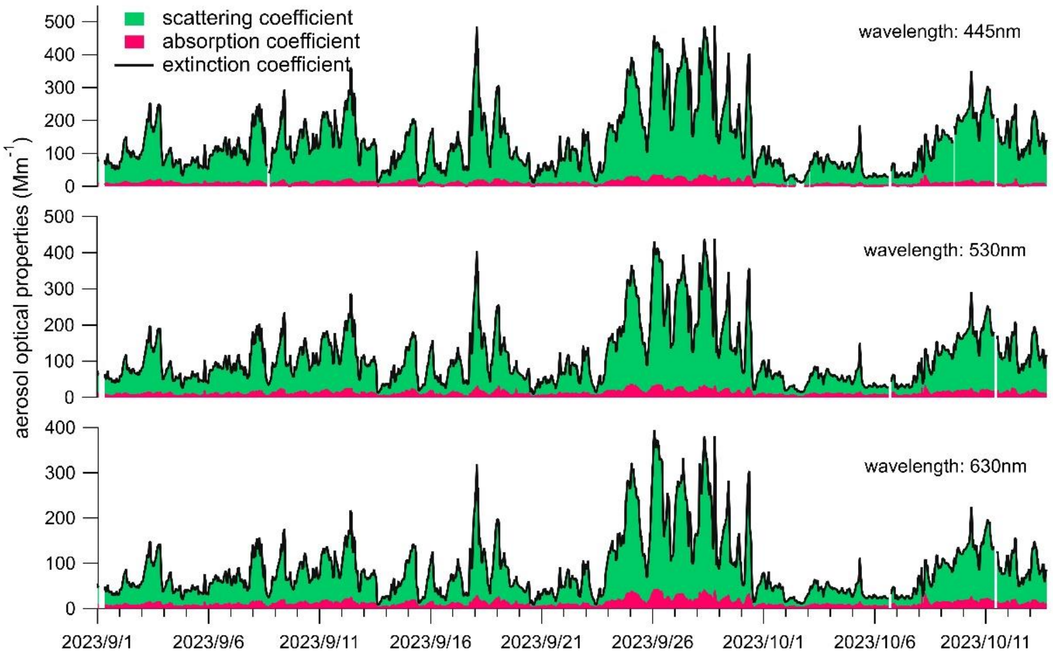

Figure S3. The scattering coefficient, absorption coefficient and extinction coefficient of particles were measured by CAPS-ALB at wavelength of 445 nm, 530 nm and 630 nm.

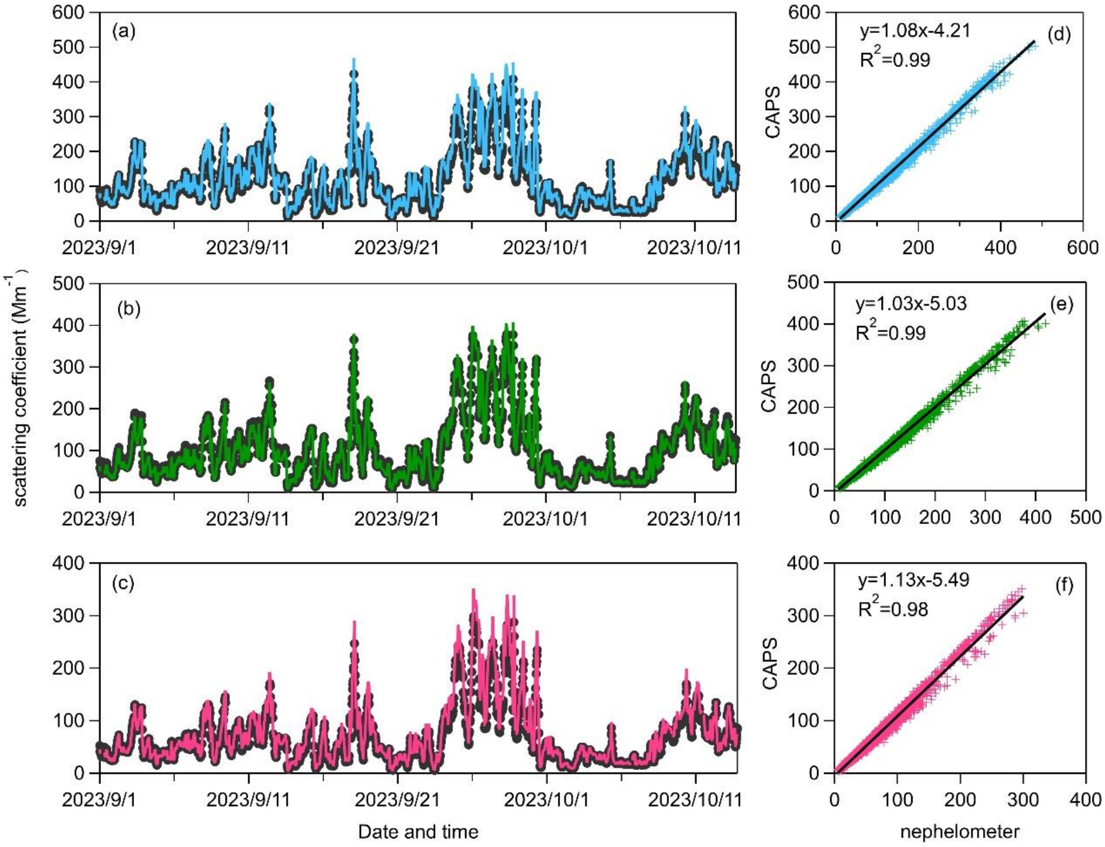

Figure S4. Comparisons of the scattering coefficients measured by CAPS-ALB at wavelengths of 445 nm, 530 nm, and 630 nm, and by the nephelometer at wavelengths of 450 nm, 525 nm, and 635 nm.

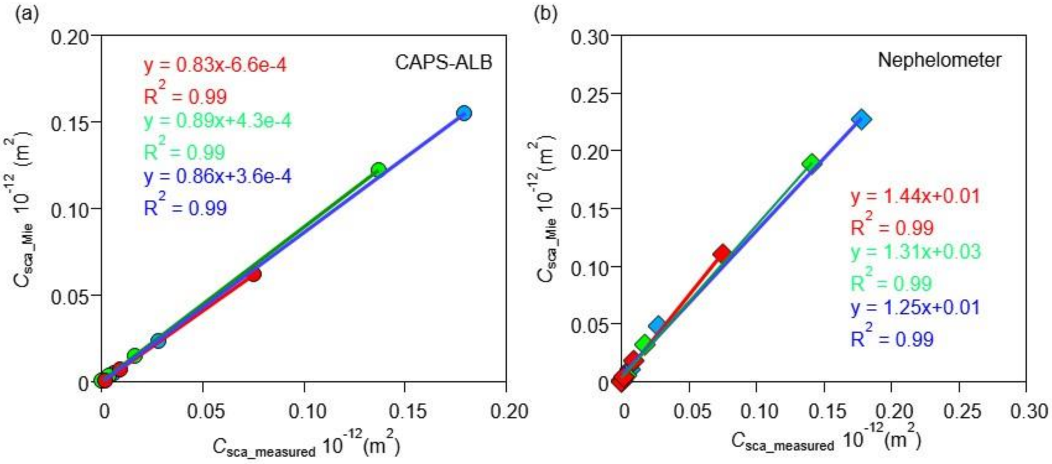

Figure S5. The scattering cross section ($C_{\text{sca\_measured}}$) measured by CAPS-ALB (a) and the Nephelometer (b) are compared with those modeled using Mie theory ($C_{\text{sca\_Mie}}$).

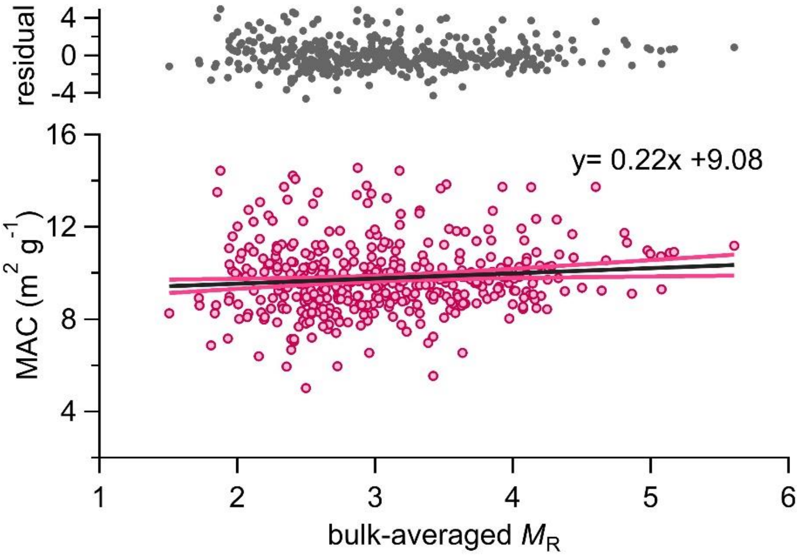

Figure S6. The relationship between MAC and bulk-averaged M_R at λ=630 nm is shown, with fitted lines and their associated 90th confidence intervals. The extrapolated MAC value for pure BC (MAC_{BC_core}) at a bulk-averaged M_R of 0 is 9.08 m^2 g^{-1} ± 0.53 m2 g-1 (mean ± 90% confidence Interval). The horizontal pink dashed lines indicate the upper and lower bounds of the 90% confidence interval of the fitted curve. The grey dots were the residual from the fits.

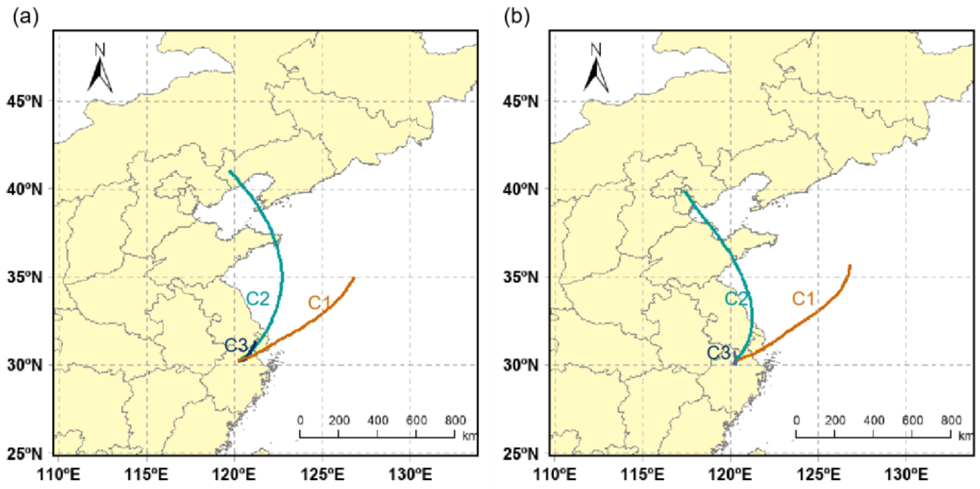

Figure S7. 48-hour backward trajectories of air masses during all observation periods at 100 m, 500 m, and 1000 m above ground level, calculated using the Hybrid Single-Particle Lagrangian Integrated Trajectory (HYSPLIT) model driven by GDAS meteorological fields.

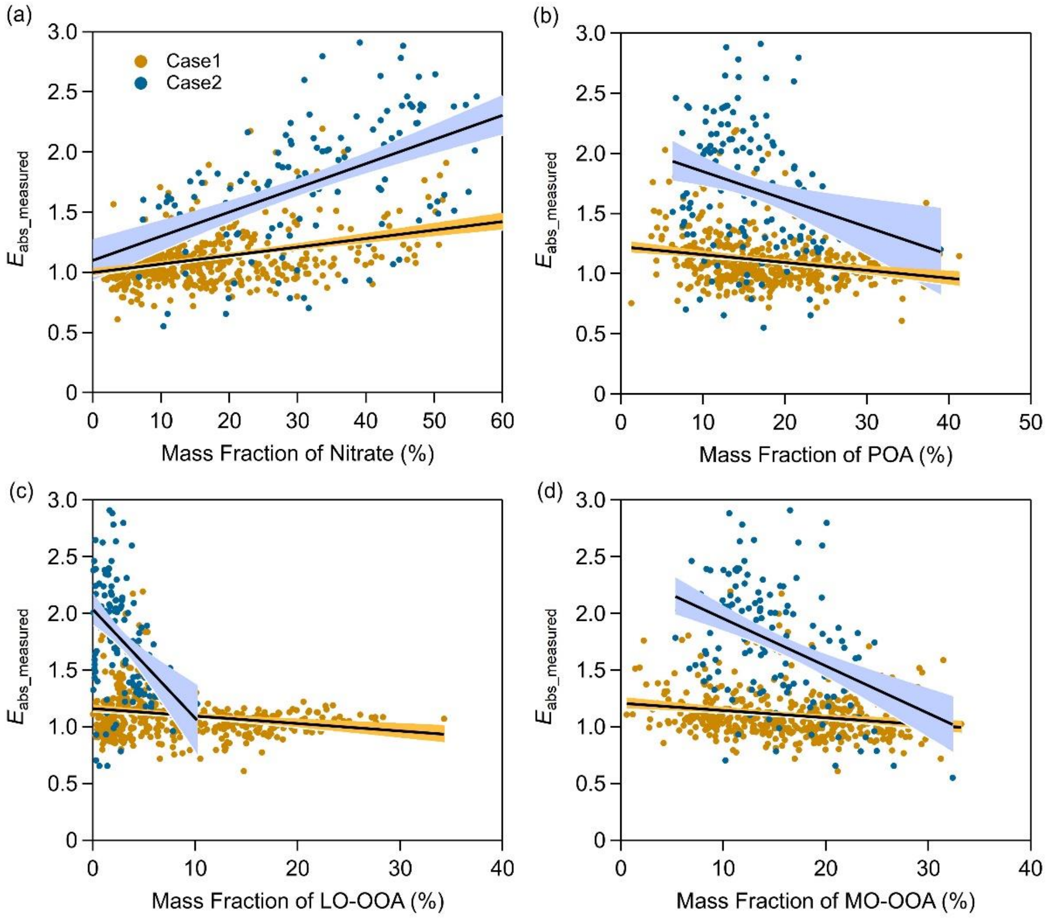

Figure S8. The relationship between measured E_{abs} and the mass fraction of nitrate (a), POA (b), LO-OOA (c), and MO-OOA (d) during Case 1 and Case 2. The black solid line represents the fitted curve, and the shaded area indicates the 90% confidence interval of the fit. Note that the chemical composition of particles was not measured during Case 3, and thus no analysis was conducted for this case.

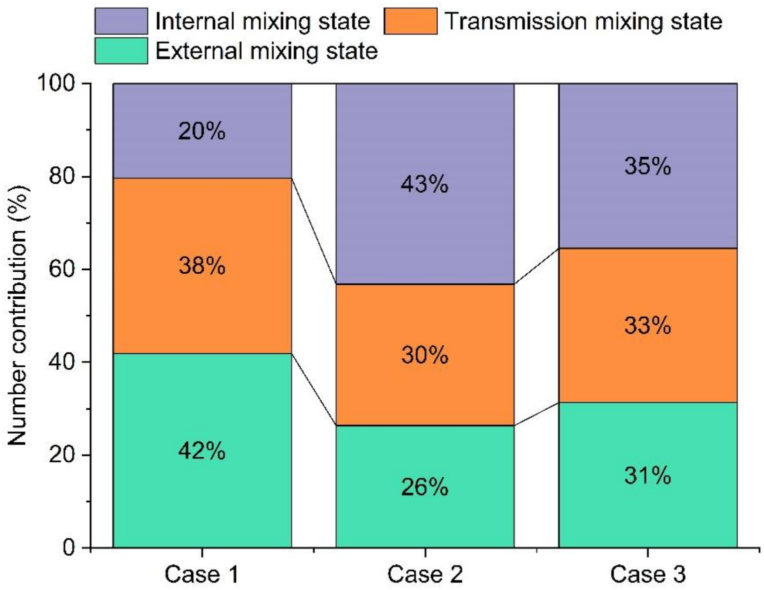

Figure S9. The proportions of externally mixed, transitional, and internally mixed BC-containing particles based on CPMA-SP2 measurement during different cases.

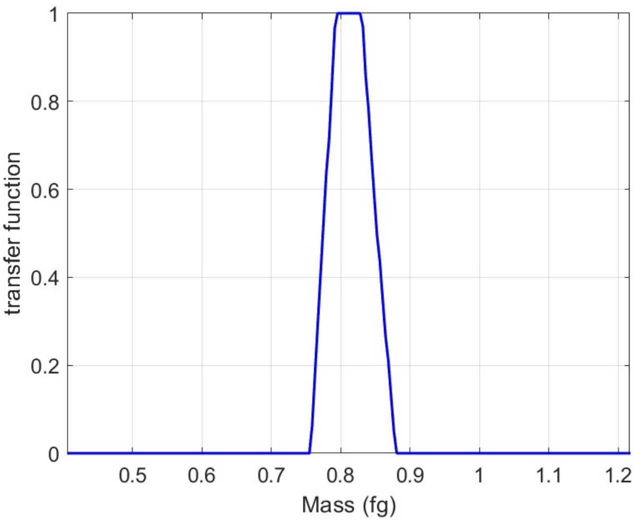

Figure S10. The transfer function of CPMA

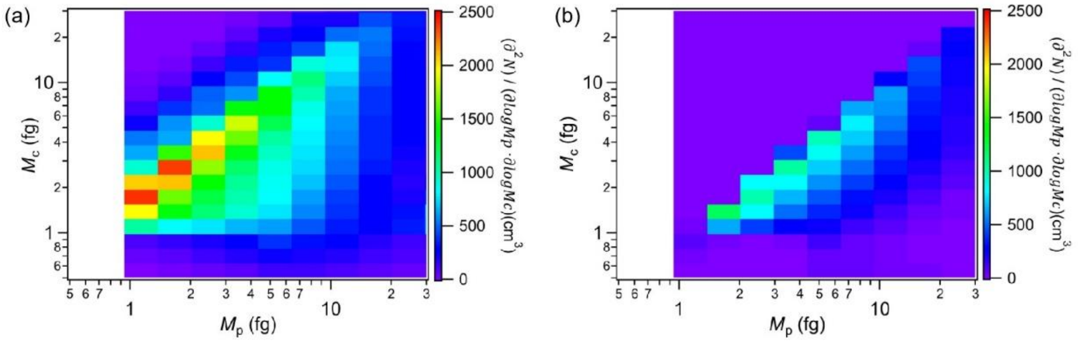

Figure S11. Multiple charging diagnostics in the tandem CPMA-SP2 system. (a) presents the number distribution of M_c-M_p before removing the BC-containing particles affected by multiple charging. (b) displays the number distribution of M_c-M_p after removing the BC-containing particles affected by multiple charging.

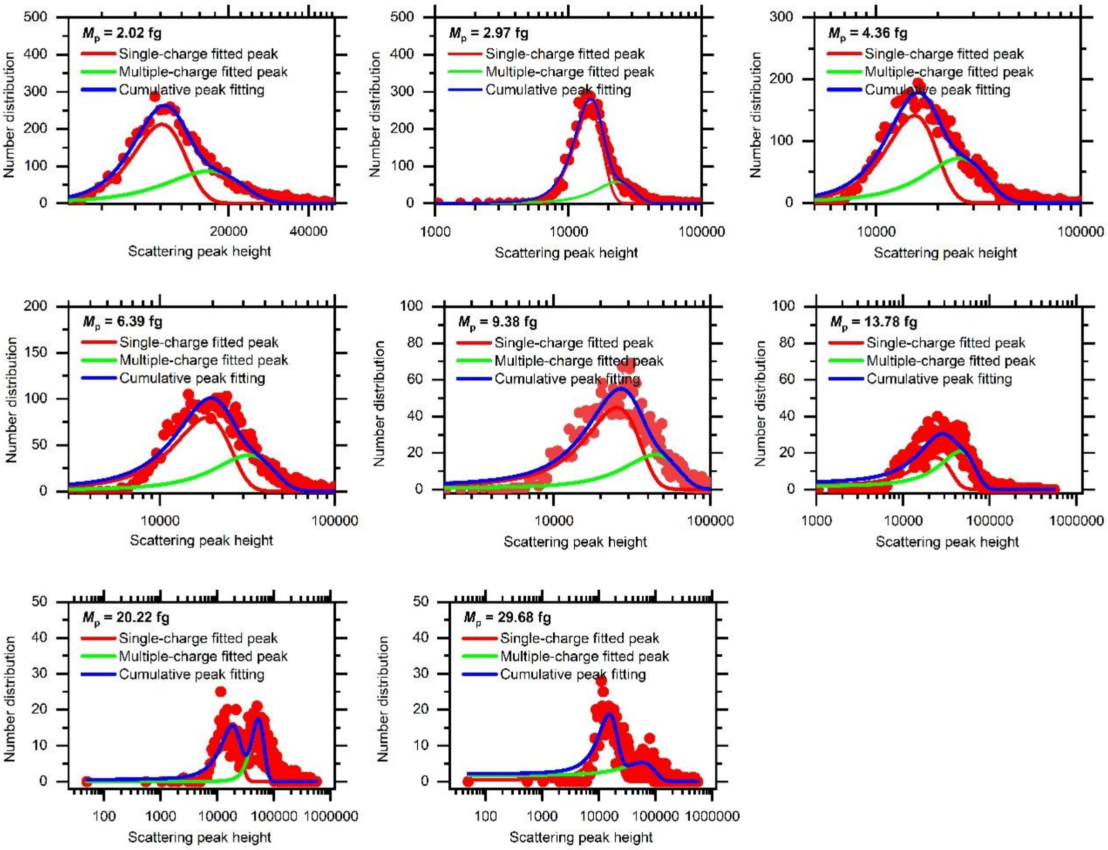

Figure S12. Multiple charging diagnostics in the tandem CPMA-SP2 system. The number distribution of scattering-signal peak heights at each selected M_p was fitted using a bimodal Gaussian function, with one peak representing singly charged particles and the other corresponding to doubly charged particles. The intersection point of the two fitted peaks was used as the threshold for distinguishing singly from doubly charged particles at that M_p, enabling a quantitative evaluation of multiple charging effects.

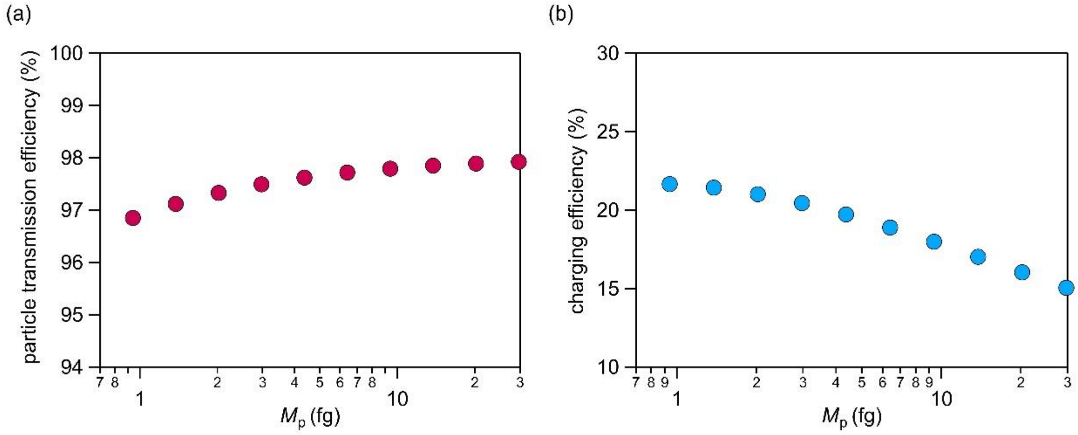

Figure S13. Mass-dependent charging efficiency of singly charged BC-containing particles and the associated tubing loss.

References:

Cappa, C. D., Zhang, X., Russell, L. M., Collier, S., Lee, A. K. Y., Chen, C. L., Betha, R., Chen, S., Liu, J., Price, D. J., Sanchez, K. J., McMeeking, G. R., Williams, L. R., Onasch, T. B., Worsnop, D. R., Abbatt, J., and Zhang, Q.: Light Absorption by Ambient Black and Brown Carbon and its Dependence on Black Carbon Coating State for Two California, USA, Cities in Winter and Summer, Journal of Geophysical Research: Atmospheres, 124, 1550-1577, 10.1029/2018JD029501, 2019.

Cappa, C. D., Onasch, T. B., Massoli, P., Worsnop, D. R., Bates, T. S., Cross, E. S., Davidovits, P., Hakala, J., Hayden, K. L., Jobson, B. T., Kolesar, K. R., Lack, D. A., Lerner, B. M., Li, S.-M., Mellon, D., Nuaaman, I., Olfert, J. S., Petäjä, T., Quinn, P. K., Song, C., Subramanian, R., Williams, E. J., and Zaveri, R. A.: Radiative Absorption Enhancements Due to the Mixing State of Atmospheric Black Carbon, Science, 337, 1078-1081, https://doi.org/10.1126/science.1223447, 2012.

Fuchs, N. A., Stechkina, I. B., and Starosselskii, V. I.: On the determination of particle size distribution in polydisperse aerosols by the diffusion method, British journal of applied physics, 13, 280-281, 10.1088/0508-3443/13/6/307, 1962.

Gormley, P. G. and Kennedy, M.: Diffusion from a Stream Flowing through a Cylindrical Tube, Proc. R. Ir. Acad., Sect. A. 52, 163-169.1984.

Huang, X.-F., Peng, Y., Wei, J., Peng, J., Lin, X.-Y., Tang, M.-X., Cheng, Y., Men, Z., Fang, T., Zhang, J., He, L.-Y., Cao, L. M., Liu, C., Zhang, C., Mao, H., Seinfeld, J. H., and Wang, Y.: Microphysical complexity of black carbon particles restricts their warming potential, One Earth, 7, 10.1016/j.oneear.2023.12.004, 2024.

Peng, J., Hu, M., Guo, S., Du, Z., Zheng, J., Shang, D., Zamora, M. L., Zeng, L., Shao, M., Wu, Y.-S., Zheng, J., Wang, Y., Glen, C. R., Collins, D. R., Molina, M. J., and Zhang, R.: Markedly enhanced absorption and direct radiative forcing of black carbon under polluted urban environments, Proceedings of the National Academy of Sciences, 113, 4266-4271, 10.1073/pnas.1602310113, 2016.

Sipkens, T. A., Olfert, J. S., and Rogak, S. N.: Inversion methods to determine two-dimensional aerosol mass-mobility distributions II: Existing and novel Bayesian methods, Journal of Aerosol Science, 146, 105565, https://doi.org/10.1016/j.jaerosci.2020.105565, 2020a.

Sipkens, T. A., Olfert, J. S., and Rogak, S. N.: New approaches to calculate the transfer function of particle mass analyzers, Aerosol Science and Technology, 54, 111-127, 10.1080/02786826.2019.1680794, 2020b.

Zhai, J., Yang, X., Li, L., Bai, B., Liu, P., Huang, Y., Fu, T.-M., Zhu, L., Zeng, Z., Tao, S., Lu, X., Ye, X., Wang, X., Wang, L., and Chen, J.: Absorption Enhancement of Black Carbon Aerosols Constrained by Mixing-State Heterogeneity, Environmental Science & Technology, 56, 1586-1593, 10.1021/acs.est.1c06180, 2022.

Zhao, G., Tan, T., Zhao, W., Guo, S., Tian, P., and Zhao, C.: A new parameterization scheme for the real part of the ambient urban aerosol refractive index, Atmospheric Chemistry and Physics, 19, 12875-12885, 10.5194/acp-19-12875-2019, 2019.